communications earth & environment

Article

https://doi.org/10.1038/s43247-024-01968-6

Recent ice melt above a mantle plume track is accelerating the uplift of Southeast Greenland

Maaike F. M. Weerdesteijn [1,2] ✉ & Clinton P. Conrad [2,3]

Around the periphery of the Greenland ice sheet, satellite-based observations of ground uplift record Earth's response to past and recent unloading of Greenland's ice mass. On the southeast coast, near the Kangerlussuaq glacier, rapid uplift exceeding 12 mm/yr cannot be explained using current layered Earth deformation models. Here we find that 3D models with a weakened Earth structure, consistent with the passage of Greenland over the Iceland plume, can explain the rapid uplift of Southeast Greenland. This uplift is dominated by a viscous response that is accelerated by the low viscosities of the hot plume track. Recent mass loss, occurring during the last millennium and especially within the past few decades, drives most of the uplift. Holocene indicators recorded similarly rapid uplift following deglaciation that ended the last ice age. Such rapid uplift, occurring beneath marine terminating glaciers, can affect the future stability of entire ice catchment areas and will become increasingly important in the near future as deglaciation accelerates.

The solid Earth beneath the Greenland ice sheet is deforming due to past and present changes in ice loading, as part of a process called glacial isostatic adjustment (GIA)[1]. Around most of Greenland's periphery, this deformation is currently observed as slow uplift of the ground surface (few mm/yr) in response to deglaciation of the ice sheet[2,3]. However, on the coast of Southeast Greenland, near the Kangerlussuaq glacier, several Global Navigation Satellite System (GNSS) stations show unusually rapid uplift exceeding 12 mm/yr[3,4] (Fig. 1B) that cannot be explained by current GIA models[2,5,6], even with effective transient viscosity[6]. One explanation for this rapid uplift may arise from Greenland's unusual tectonic history: Greenland passed over the Iceland mantle plume over 40 Myr ago[7–9], and it is likely that the traces of this plume-lithosphere interaction are preserved beneath Southeast Greenland[10,11]. Magnetic, heat flow, gravity, radar, and seismic data[9,10,12–17] point towards a potentially thinner lithosphere and weakened upper mantle beneath parts of Southeast Greenland. Recent studies suggest that a weakened Earth structure can dramatically accelerate the viscoelastic response to deglaciation, leading to rapid uplift beneath regions of active present-day mass loss[3,18–20]. Indeed, rapid uplift above a low-viscosity region associated with the Iceland plume has been proposed[3], but this hypothesis has not been tested in a 3D setting[18], nor with all of the relevant ice mass changes that have occurred within the last glacial cycle, the most recent millennium, and the past few decades. Deglaciation on all these timescales has been shown to impact present-day uplift patterns[6].

Full 3D modelling of GIA deformation is computationally challenging because uplift is driven by glacial loads from both distant and nearby sources[1]. Distant loads drive long-wavelength deformation (thousands of km) that is sensitive to Earth's overall stratified viscosity structure[21] while local loads drive regional deformation (tens of km) that is sensitive to the local viscosity structure nearby[18,22]. We have overcome the challenge of modelling across these disparate scales by combining global models of large-scale deformation with high-resolution models of regional deformation. For the regional modelling, we utilize a new viscoelastic modelling tool in ASPECT (Advanced Solver for Problems in Earth's ConvecTion)[23–28] that can handle large lateral viscosity variations across short length scales, which enables high-resolution modelling on regional scales. We used this new code to develop regional deformation models for Southeast Greenland (see model setup in Fig. 1 and description in "Methods") in combination with ice loading changes across the last glacial cycle (ice loading since 122 ka bp)[21,29], the second millennium (1000–1995 AD)[6], and the recent satellite altimetry era (1992–2020 AD)[30]. Within these regional models, we investigated the influence of weakened Earth structure along a "plume track" that is 100 s of km wide and follows the expected path of Greenland over the Iceland Plume before 40 Ma[7–9]. We combined these global and regional deformations (see "Methods") to model uplift rates in Southeast Greenland, which we subsequently compared to observed rates of present-day uplift from GNSS and Holocene relative sea level (RSL) drop.

[1]Department of Geophysics, University Centre in Svalbard, Longyearbyen, Norway. [2]Centre for Earth Evolution and Dynamics, University of Oslo, Oslo, Norway. [3]Centre for Planetary Habitability, University of Oslo, Oslo, Norway. ✉e-mail: maaikew@unis.no

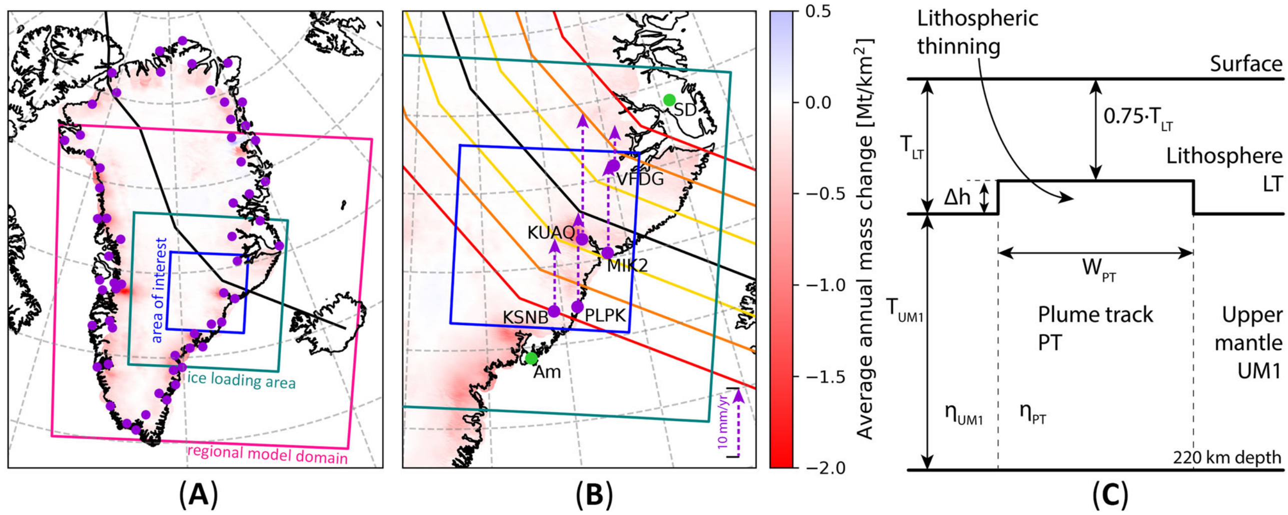

Fig. 1 | Southeast Greenland and plume track modelling. A Map of Greenland showing the average annual ice mass change over 1992-2020 from VMB data (background colors), 60 GNET GNSS stations (purple dots), the regional model domain (pink box), the ice loading area (teal box), the area of interest (blue box), and the potential plume track, drawn following Martos et al.[9] (black line). **B** The same as (**A**) but zoomed to show five GNET GNSS stations and their acronyms, the observed uplift rates (purple arrows), two Holocene sea level sites and their abbreviations (green dots), and the boundaries of plume tracks with widths of 200 km (yellow), 400 km (orange), and 600 km (red). **C** A cross-section of the Earth model showing the plume track, which extends from the base of the lithosphere (LT) to the base of the upper mantle layer (UM1) (Table S3). T denotes the layer thickness, Δh the lithospheric thinning, η the viscosity, and W_{PT} the plume track width.

Our regional GIA modelling across timescales ranging from thousands of years to decades emphasizes the importance of lateral variations in rheology consistent with those expected for the Iceland plume track. In particular, we demonstrate that localized regions of unusually rapid uplift occur where rapid deglaciation is positioned above pockets of mantle with diminished linear viscosity and thin lithosphere. We have identified one such region along the coastline of Southeast Greenland, where uplift faster than 2 cm/yr was sustained for ~2000 years in the Early Holocene and is today observed in excess of 17 mm/yr near the rapidly retreating Kangerlussuaq glacier. This uplift is accelerated compared to other coastal areas of Greenland because the mantle beneath Southeast Greenland has been weakened by interaction with the Iceland plume.

Results and discussion

Models and observations of uplift in Southeast Greenland

We construct high-resolution regional models (see "Methods") of solid Earth deformation in Southeast Greenland for a region (Fig. 1A, pink box) that includes an ice loading area (Fig. 1A, teal box), our primary area of interest (Fig. 1A, blue box), and an imposed plume track (Fig. 1A, black line). Within the chosen width of the plume track (Fig. 1B, colored lines) we assign reduced mantle viscosity and thinner lithosphere (see "Methods" and Fig. 1C), consistent with thermal weakening caused by earlier passage of the Iceland Plume (see "Methods"). Three uplift rates are computed, based on deformation driven by deglaciation over the (1) last glacial cycle, (2) second millennium, and (3) satellite altimetry era (see "Methods"). We additionally use global models to compute the component of uplift caused by distant deglaciation (occurring outside our ice loading area) during the (4) last glacial cycle and (5) recently (2009–2020). The total modeled uplift is thus the sum of these 5 contributions.

We compare modeled uplift with observations of recent uplift measured at 5 GNSS stations in Southeast Greenland (Fig. 1B). These stations show uplift at rates ranging from 5 to 17 mm/yr, with the fastest uplift occurring at Kangerlussuaq Glacier (station KUAQ). We also compare with uplift rates from the early Holocene uplift, as measured at two locations in Southeast Greenland. These are Schuchert Dal (SD)[31], located in (currently deglaciated) Jameson Land to the north, and Ammassalik (Am)[32], located southeast of the Helheim glacier to the south (Fig. 1B). Geologic indicators of sea level change at SD and Am indicate ground uplift at rates of 28 and 24 mm/yr, respectively, between about 11 and 8 thousand years ago (see "Methods").

Patterns of uplift near the plume track for different deglaciation timescales

We first consider the solid Earth response to last glacial cycle loading, which drives present-day uplift in Southeast Greenland and subsidence across interior Greenland (Fig. S1 and Table S1). If a low-viscosity plume track is included in the models, return flow from this subsidence drives uplift along the plume track (Fig. S2). At the GNSS sites, uplift rates are only a few mm/yr (Table S2.iii) and are rather insensitive to variations in plume track characteristics and lithospheric thickness (Fig. S2). For times in the past, however, vertical displacement rates depend on the plume track characteristics (Figs. 2, S3 and S4), and this dependence is largest during times of rapid ice mass change (e.g., between 10 and 4 ka bp, Fig. S5A). Over the last deglaciation, GNSS site VFDG was especially sensitive to the lithosphere thickness and track properties, with uplift reaching over 60 mm/yr at ~9 ka bp for a wide track (Fig. 2A), a low track viscosity (Fig. S3A), or a thin lithosphere (Fig. S4A). This is not the case for the present-day rates (Fig. 3A) because ice loading has been minimal during the past few thousand years (Fig. S5) and low plume track viscosities create a short GIA response time (hundreds of years, Fig. S6). Thus, uplift occurs soon after the melting, and is already exhausted by the present-day. This rapid past uplift was recorded by Holocene relative sea level indicators at SD and Am (Fig. 2B). Our models predict uplift rates at these locations that are slower than observed (Fig. 2B), and only slightly affected by the plume track width (Fig. 2B), plume track viscosity (Fig. S3B), or lithospheric thickness (Fig. S4B). This is likely because both SD and Am lie outside of the plume track (Fig. 1B). We will revisit Holocene uplift at these sea level sites below, where we consider the horizontal extent of the low-viscosity region.

In response to second millennium deglaciation, our regional models predict much faster present-day uplift, but only along the low-viscosity plume track (Fig. 3B). Outside the plume track, deformation is minimal (less than 1 mm/yr). This is because the mantle response to second millennium deglaciation is mostly sensitive to the viscosity of the shallow asthenosphere[33], resulting in uplift patterns confined to short wavelengths (100 s of km) corresponding to asthenospheric depths. Within the plume track, the largest predicted uplift rates occur for a thin elastic lithosphere (rates up to 11.2 mm/yr), or for a low viscosity or wide plume track (rates up to 6.3 mm/yr) (Figs. S6, S7). Our models predict regions of subsidence along the plume track to the NW and SE. These peripheral bulges occur on both sides of the rapidly uplifting region, in a pattern similar to that of Earth's

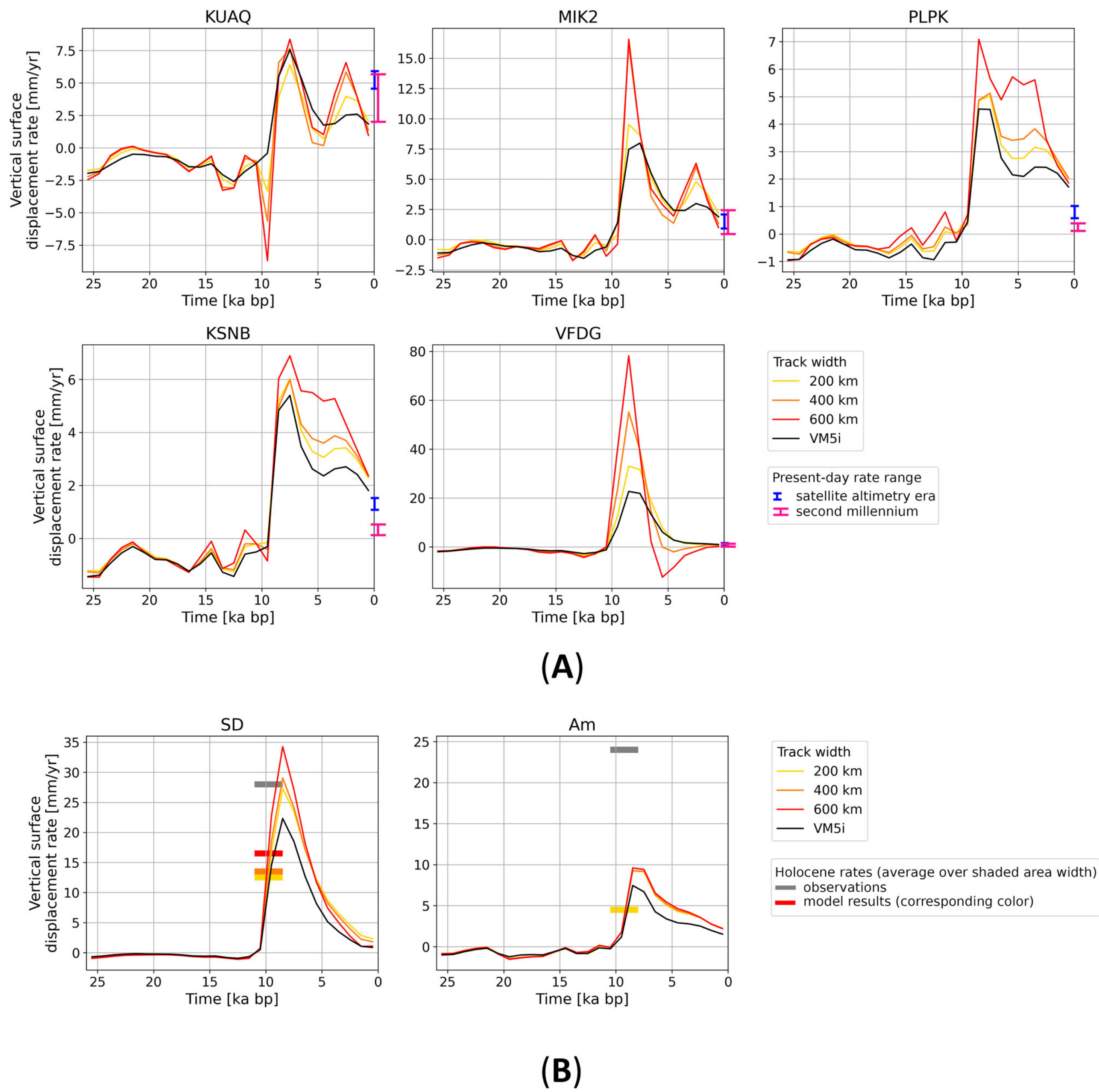

Fig. 2 | Uplift rates due to last glacial cycle ice loading for different plume track widths. Vertical surface displacement rates since the last glacial maximum for plume track widths of 200 km (yellow), 400 km (orange), 600 km (red), a track viscosity of $1 \cdot 10^{19}$ Pa s, and a 60 km lithospheric thickness outside the plume track (**A**) for the five GNSS sites and (**B**) for the two sea level sites. Shown for comparison are results for the layered VM5i rheological model without a plume track (black), ranges of present-day rates induced by ice loading changes over the satellite altimetry era (blue bar) and second millennium (pink bar) in (**A**), and ranges of Holocene uplift rates based on observations (grey bar) and model results (colored bars) in (**B**), for the Earth models with a plume track considered here.

response to longer-wavelength deglaciation of the Laurentide ice sheet. For second millennium loading, however, this pattern occurs on shorter spatial and temporal scales and only along the low-viscosity plume track.

Deglaciation during the past few decades (satellite altimetry era) also drives rapid uplift (Fig. 3C), especially near the Kangerlussuaq glacier (stations KUAQ and MIK2). This uplift is larger than we find in models without a plume track (layered VM5i model), for which solid Earth deformation is dominantly elastic with modest uplift rates of a few mm/yr (bottom row of Fig. S8). Rapid uplift within the plume track thus represents a viscous response that is amplified by the weakened Earth structure. As for the second millennium loading, uplift rates are larger for lower track viscosity, wider track width, and thinner lithospheric thickness (Fig. S8). Of these, track viscosity has the largest impact on uplift rates, which can reach over 20 mm/yr (Figs. S8, S9). The GNSS stations on the edges of the plume track (VFDG, KSNB, and PLPK) do not show the same sensitivity to the plume track characteristics (Fig. S9 and Table S2.v). This suggests that the greatest uplift rates occur near rapidly deglaciating regions that are positioned over low-viscosity regions of the upper mantle, as previously shown in idealized models[18].

Uplift rates of the Southeast Greenland GNSS sites constrain plume track characteristics

For a reference plume track of 400 km width, $1 \cdot 10^{19}$ Pa s viscosity, and lithospheric thickness of 60 km (Fig. 3), widespread deglaciation of the last glacial cycle drives uplift along the entire southeast coast (Fig. 3A). By contrast, second millennium and the satellite altimetry era melting generate

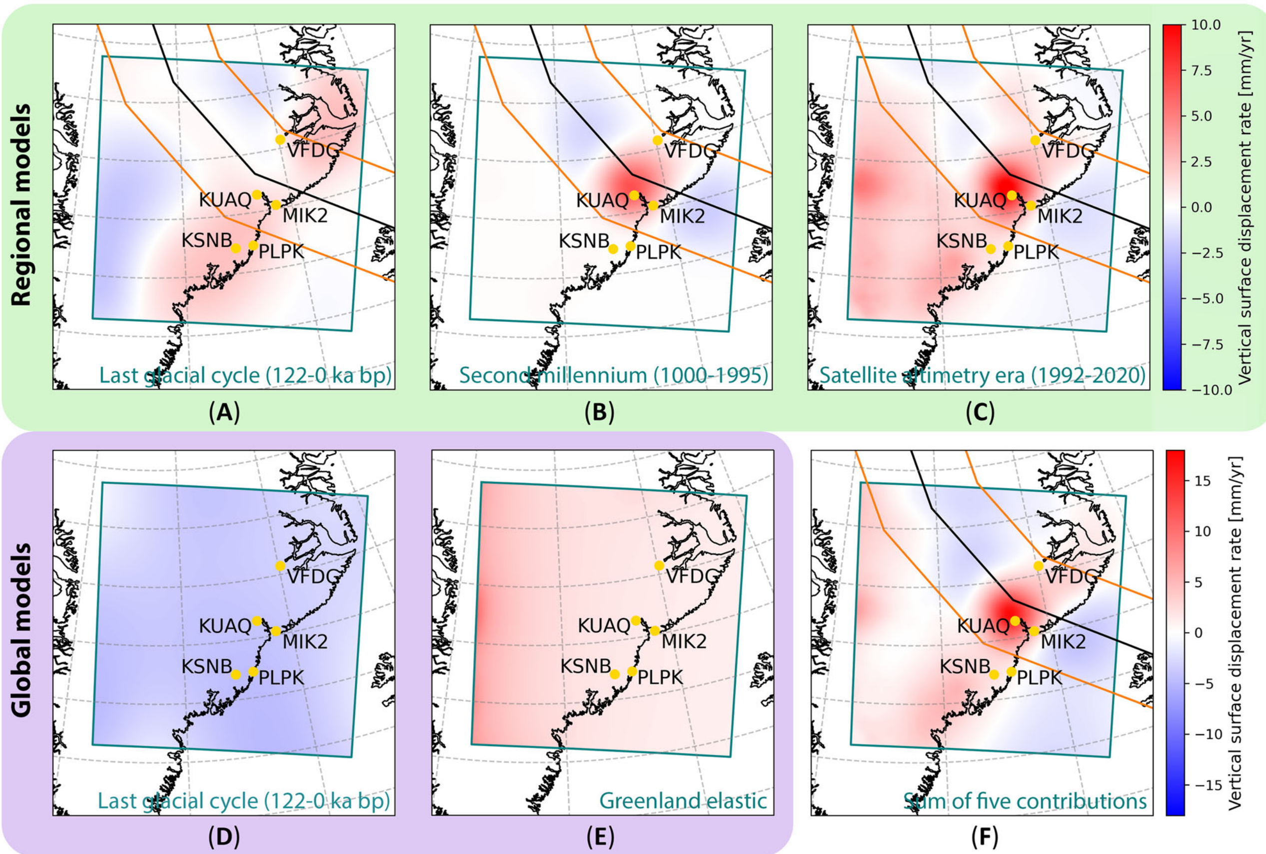

Fig. 3 | Predicted present-day uplift rates from five contributors and the total. The five contributors are computed from high-resolution regional modelling (top row, green shaded background) of Earth deformation driven by ice mass changes during the (**A**) the last glacial cycle, (**B**) the second millennium, and (**C**) the satellite altimetry era, and global modelling that excludes regional ice and lateral viscosity variations (bottom row, purple shaded background) of (**D**) Earth deformation driven by last glacial cycle ice loading changes and (**E**) Earth's elastic response to contemporary ice loading changes over Greenland. **F** The sum of the five contributors, with the five GNSS sites (yellow dots), ice loading area (teal box), plume track (black line), and plume track boundaries (orange lines). The regional modelling is performed for Earth model VM5i as described in Table S3, employing as a reference model a lithospheric thickness of $T_{\mathrm{LT}} = 60$ km and a plume track 400 km wide that contains thinned lithosphere and viscosity $\eta_{\mathrm{PT}} = 1 \cdot 10^{19}$ Pa s (constructed as in Fig. 1C).

uplift that is fastest within the plume track (Fig. 3B, C). Greenland's location on the collapsing peripheral bulge of the Laurentide ice sheet is associated with slow subsidence (Fig. 3D and Table S2.i), and the elastic response to contemporary ice melt over the rest of Greenland (outside the defined ice loading area) generates widespread minor uplift (Fig. 3E and Table S2.ii). The combined total vertical surface displacement rates (Fig. 3F) thus show patterns and magnitudes that are dominantly driven by ice loading changes since 1000 AD.

For a variety of plume track models, we see large variations in uplift rates along Greenland's east coast, peaking near the Kangerlussuaq glacier (Fig. 4). This is in part due to large recent ice mass loss there, which drives uplift that is amplified by the low-viscosity plume track. A wider plume track results in a wider region of rapid uplift and also faster uplift. Our reference model predicts uplift rates faster than 10 mm/yr near the Kangerlussuaq glacier (Fig. 3F), but these rates increase to over 20 mm/yr for a thinner lithosphere or lower plume track viscosity (Fig. 4). By contrast, the layered VM5i model, which employs a uniform upper mantle viscosity of $5 \cdot 10^{20}$ Pa s (Table S3) without a plume track, shows much slower uplift along the coast that is dominated by an elastic response to recent deglaciation (Fig. 4, bottom row). The total modeled uplift rates for all combinations of our Earth model properties (Fig. 5) show that we can match observations of uplift rates at KUAQ, MIK2, and VFDG with a wide and low-viscosity plume track. In combination with a thin lithosphere (30 km), a model with a broad and weak track greatly overestimates uplift rates at KUAQ, but shows a good match at MIK2 and VFDG. However, our models underpredict uplift rates at PLPK and KSNB, as uplift at these locations to the south seems to be insensitive to the choice of plume track (Figs. 5, S10, and S11).

Uplift rates driven by remote deglaciation on all timescales (Fig. 3D, E) show little variation across Southeast Greenland. Instead, present-day uplift rates at the GNSS sites are mostly affected by local and recent ice loading changes, as inferred for Southeast Greenland during the satellite altimetry era and the second millennium. The dominance of this recent mass loss is evident spatially (Fig. 3) and in magnitude, but only for locations positioned above a broad and weak plume track (compare Figs. 6, S12, S10, S11, and S13). This viscous uplift from recent and local ice melt is not usually considered in GIA models, which typically model global deformation on longer wavelengths and longer timescales. Yet, our models predict that future solid Earth deformation will become increasingly driven by recent and local ice melt as deglaciation accelerates.

Coastal extent of the low-viscosity region

Our models with a plume track cannot match observed uplift rates at two GNSS stations south from the Kangerlussuaq glacier, PLPK and KSNB. Uplift at these GNSS sites seems to be insensitive to the choice of plume track, and we predict slower uplift rates than observed. Even when the plume track extends to these sites (e.g., for a 600 km wide plume track), uplift rates are barely affected. It is possible that the VMB constraints on mass loss in the southern part of the ice loading area may not capture the full extent of the ice mass loss there. Constraints on recent mass changes are especially important in our models because we also use them to infer the spatial pattern of second millennium mass changes. Furthermore, ice mass changes along the ice

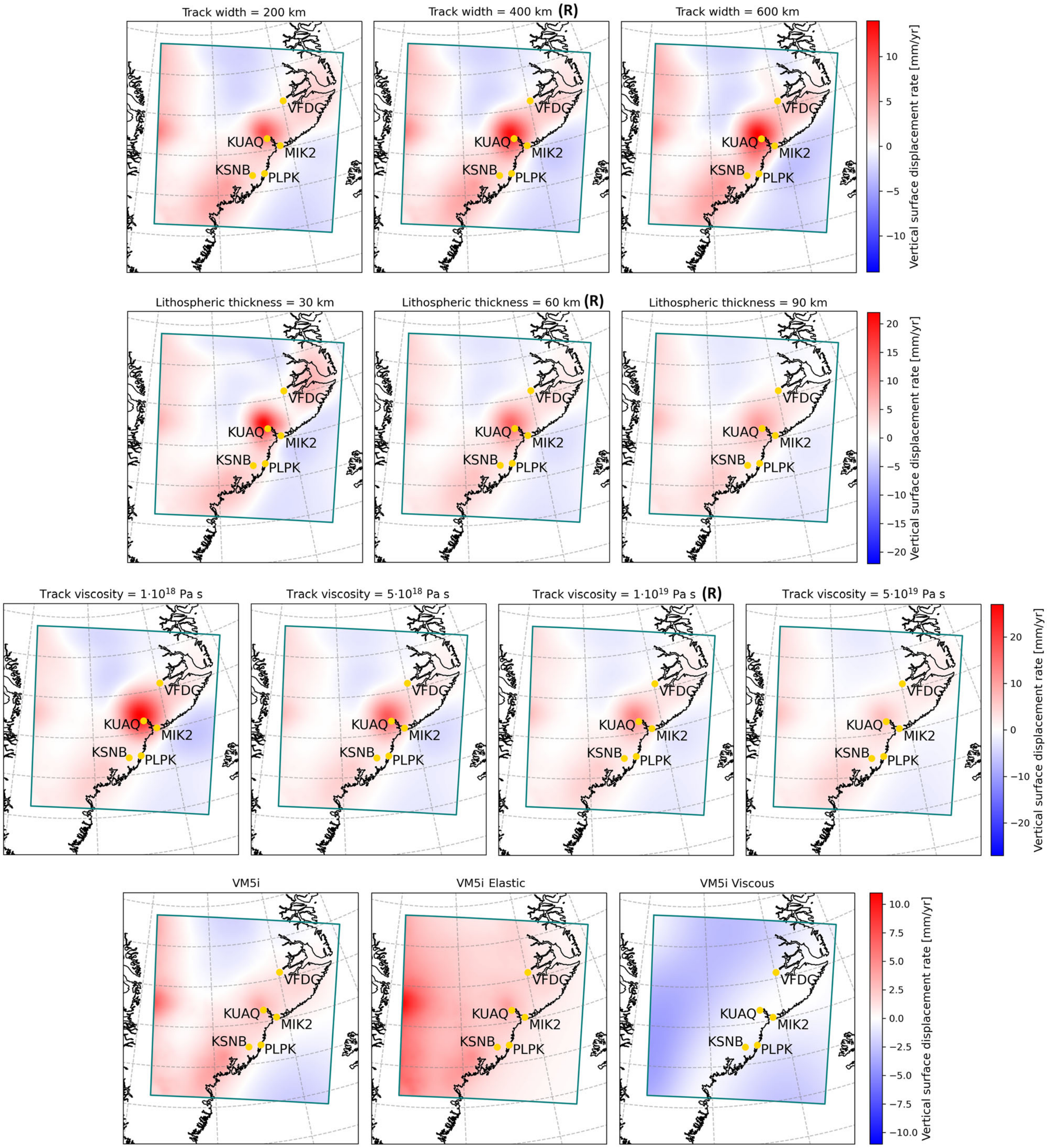

Fig. 4 | Total uplift rates across Southeast Greenland for different plume track models. Deformation produced by the five contributions summed together (as for Fig. 3F) and shown for the present day over Southeast Greenland with the five GNSS sites (yellow dots) and imposed plume tracks (as in Fig. 1B). Panels show variations from a reference model with a lithospheric thickness of $T_{\mathrm{LT}} = 60$ km and a plume track of width of 400 km and viscosity $\eta_{\mathrm{PT}} = 1 \cdot 10^{19}$ Pa s. Variations to this model include plume track widths of 200 km, 400 km, and 600 km (top row), lithospheric thicknesses of 30 km, 60 km, and 90 km (second row), and plume track viscosities of $1 \cdot 10^{18}$ Pa s, $5 \cdot 10^{18}$ Pa s, $1 \cdot 10^{19}$ Pa s, and $5 \cdot 10^{19}$ Pa s (third row). **(R)** denotes the reference model. Also shown (bottom row) are the layered VM5i rheological model (Table S3) and the purely elastic (VM5i Elastic) and viscous (VM5i Viscous) components of the response to the ice loading.

sheet periphery are particularly difficult to estimate[34], and thus it is useful to consider alternative mass balance datasets[35,36]. For example, recent high-resolution altimetry (Fig. 12 of Khan et al.[36]) generally predicts larger annual mass change rates after 2017 compared to the model used here. The higher resolution of that dataset (1 km as opposed to 5 km used here), however, would not improve our solid Earth deformation models, which use 6 km as the finest mesh resolution. Similarly, a more focused Greenland ice history model[37] may provide better constraints over the last glacial cycle than the global model that we used. However, we have already shown that mass loss during the last glacial cycle is less important than more recent ice mass changes, because the latter drive most of the deformation above low-viscosity regions.

South of the PLPK and KSNB stations lies the Helheim glacier (within our ice loading area but not within the plume track), one of Greenland's three largest glaciers based on catchment size, and also deglaciating rapidly[38]. If the weakened Earth structure of the plume track extends

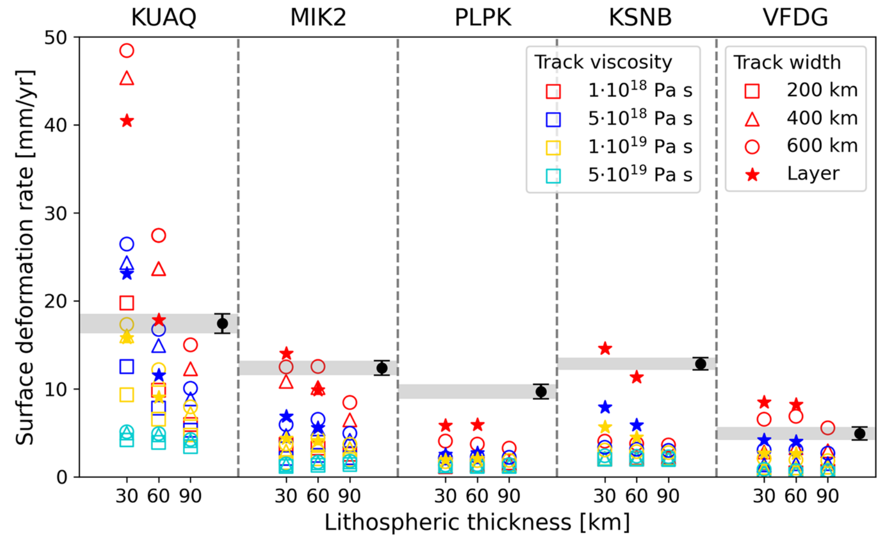

Fig. 5 | Total uplift rates at the five GNSS sites for different plume track models. Vertical surface displacement rates at five GNSS sites (KUAQ, MIK2, PLPK, KSNB, and VFDG) in response to ice loading changes (combined regional and global contributions, as for Fig. 3) from the satellite altimetry era, the second millennium, and the last glacial cycle, for Earth models with lithospheric thicknesses of 30 km, 60 km, and 90 km (*x*-axes), plume track viscosities of $1 \cdot 10^{18}$ Pa s (red), $5 \cdot 10^{18}$ Pa s (blue), $1 \cdot 10^{19}$ Pa s (yellow), and $5 \cdot 10^{19}$ Pa s (turquoise), and plume track widths of 200 km (squares), 400 km (triangles), 600 km (circles), and a full low-viscosity layer (stars, only for models with effective lithosphere thickness of 22.5 or 45 km, corresponding to 30 km and 60 km outside the plume track, and asthenosphere viscosity of $1 \cdot 10^{18}$ Pa s, $5 \cdot 10^{18}$ Pa s, or $1 \cdot 10^{19}$ Pa s, as indicated by star color). Observed uplift rates with standard deviation (black dots with error bars and corresponding grey bands) are shown for comparison.

southward to the Helheim glacier, mass loss there could increase uplift rates at PLPK and KSNB. Indeed, the lateral extent of the region weakened by the Iceland Plume is not well constrained[7,9,10,12–16,39–42], and potentially extends further south based on recent constraints from seismic tomography[14,16]. A lower viscosity in this region would reduce the resistance to material flow in the upper mantle and could lead to larger uplift rates at the PLPK and KSNB sites following ice melt of the Helheim glacier. Therefore, we also tested an Earth model in which the plume track extends further south. For simplicity, we implemented a full low-viscosity layer ($1 \cdot 10^{18}$ or $5 \cdot 10^{18}$ Pa s), by making the plume track width W_{PT} as wide as the model domain (see Fig. 1C). We tested nominally 30 and 60 km thick lithospheres, which are thinned by 25% everywhere to form effectively 22.5 and 45 km elastic lithospheres. When the low-viscosity region extends further south (Fig. 7B), we do find higher uplift rates at PLPK and we are able to match observations at KSNB near the Helheim glacier for a low-viscosity mantle ($1 \cdot 10^{18}$ Pa s) and a thin lithosphere (Fig. 5, red stars). Interestingly, when the low-viscosity area extends further south, we find lower uplift rates at KUAQ than for a more confined low-viscosity plume track. This is because the presence of low-viscosity mantle beneath both glaciers allows rapid uplift at the Helheim glacier to draw Earth material from beneath the Kangerlussuaq glacier, reducing the uplift there (Fig. 7A, B). Thus, ice mass changes at one glacier can change the force balance controlling flow beneath an adjacent glacier, if both glaciers are underlain by a common low-viscosity region.

To test the hypothesis that a weakened Earth structure extends further south and/or north, we investigate uplift rates at four additional GNSS stations (Fig. 7B), where HEL2 and KULU to the south are rising faster (8–16 mm/yr) than DGJG and SCOR to the north (2–4 mm/yr) (see "Methods"). We also consider uplift rates during the early Holocene at Schuchert Dal (SD)[31] and Ammassalik (Am)[32] (Fig. 7C, D). These six new locations lie outside the region of interest, but inside the ice loading area (Fig. 1B). Because these locations are closer to the ice loading boundary, model uplift rates may be less accurate than for the five GNSS stations inside the area of interest (see "Methods").

We find that uplift rates to the north (DGJG and SCOR) are less sensitive to the chosen Earth model than the sites to the south (HEL2 and KULU) (Fig. S14). This is because there is less recent ice melt at the northern locations, while the Helheim glacier to the south is deglaciating rapidly. HEL2, closest to the deglaciating ice, shows the largest variation in uplift rates, with the weakest layer producing the fastest rates. This suggests that rapid uplift (upwards of ~10 mm/yr) requires both rapid deglaciation and weakened asthenosphere. The GNSS observations thus suggest that the weakened region along the Southeast Greenland coastline extends further south than initially modeled (beneath HEL2 and KULU). Such models still come close to matching uplift rates within the original plume track (Fig. 5). The lack of rapid deglaciation to the north (Fig. 1B) leads to slow uplift there even above weakened mantle (Fig. 7B). This prevents us from using GNSS observations to determine the northern extent of the weakened Earth region, as both layered and plume track models produce similar uplift rates at DGJG and SCOR (Fig. S14).

Holocene sea level indicators indicate rapid uplift at both SD to the north (28 mm/yr over 11.0 to 8.5 ka bp) and Am to the south (24 mm/yr over 10.5 and 8.0 ka bp) (Fig. S15). For an Earth model with layered asthenospheric viscosity of $5 \cdot 10^{18}$ Pa s beneath effectively 22.5 km lithospheric thickness, our models predict large uplift rates at both SD to the north and Am to the south at 8.5 ka bp (Fig. 7C, note the scale). Rapid deglaciation of Jameson Land at the end of the last ice age (but not recently, as Jameson Land is currently deglaciated) explains the rapid uplift observed at SD (Fig. 7D) and predicted at VFDG (Fig. S16), and indicates that the weakened Earth region extends northward toward SD (Fig. 7C). Earth models that are uniformly weak predict modeled uplift rates at Am that are generally slower than at SD (Fig. S17), and models that match observed rates at Am tend to overpredict rates at SD (Fig. 7D). This suggests a transition to a stiffer Earth structure (i.e., higher track viscosity and/or thicker lithosphere) to the north (beyond VFDG and somewhere near SD).

On the importance of lateral viscosity variations

Although we can only test a finite number of Earth models, we find that only models with a low-viscosity feature in the upper mantle can match the observed rapid uplift near the Kangerlussuaq glacier (Fig. 5). Narrower plume tracks of width ~200 km require weak viscosities of $\eta_{PT} \sim 10^{18}$ Pa s, while wider tracks (400–600 km) can be stiffer (up to $\sim 10^{19}$ Pa s) (Fig. 6). These width estimates are consistent with geophysical observations, which also range from ~200 km[15] to 400 km[10], or even wider[14]. Models that match uplift rates near the Kangerlussuaq glacier often do not also match observed uplift rates nearby, suggesting that the complex 3D nature of the plume track may be important. Particularly, our models indicate that rapid uplift observed at stations south of the Kangerlussuaq glacier is consistent with geophysical observations that suggest an influence of the Iceland plume along this portion of the Southeast Greenland coastline[9,14,16].

Other previous studies have tried to use GNSS uplift rates to constrain Earth structure in this region. Milne et al.[5] found large discrepancies between modeled and observed uplift rates in Southeast Greenland, even though they explored the influence of a variety of low-viscosity regions with varying locations and lateral extents near the Iceland mantle plume. They explain these discrepancies by emphasizing that their models do not have the required temporal or spatial resolution to infer lateral variations on these

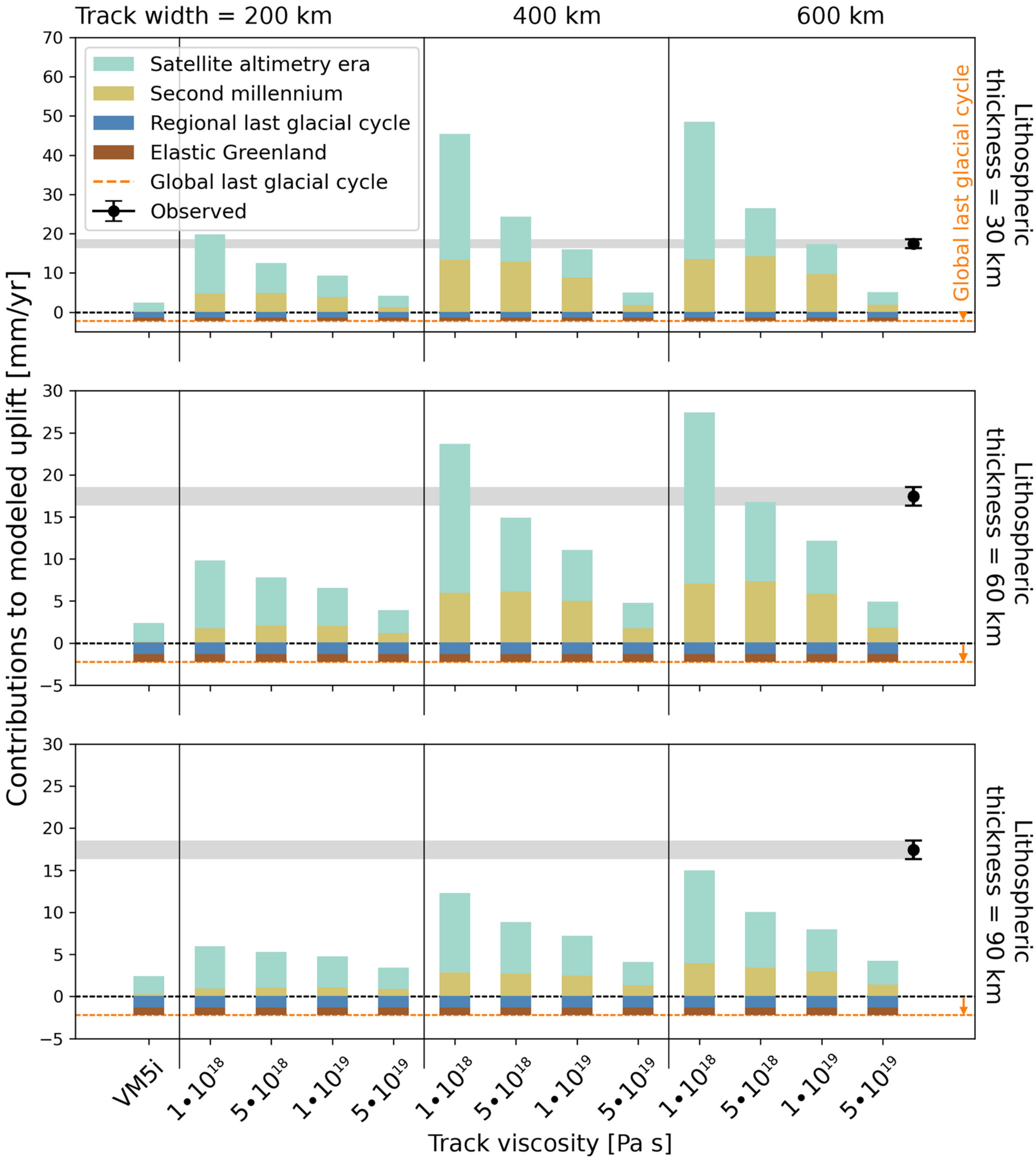

Fig. 6 | Individual contributions to uplift rates at KUAQ, for different plume track models. Contributions from regional ice loading changes over the satellite altimetry era (turquoise), the second millennium (yellow), and last glacial cycle (blue), and global models of the long wavelength elastic response to Greenland melting (brown) (Table S2.ii) and the last glacial cycle (orange arrow and dashed line, only negative contribution) (Table S2.i). The cumulative sum compares to observed uplift rates with standard deviation (black dots with error bar and grey band). Figs. S12, S10, S11, and S13 show similar comparisons for MIK2, PLPK, KSNB, and VFDG.

smaller scales. Adhikari et al.[6], using a layered viscosity model, matched GNSS uplift rates across Greenland but excluded KUAQ and MIK2 from their analysis (because of possible plume effects), and cannot match rates at PLPK and KSNB. We note that Adhikari et al.[6] and other 1D GIA modelling studies[6,37,43,44] infer or use upper mantle viscosities within 0.6 - $5 \cdot 10^{20}$ Pa s, but we show here that upper mantle viscosity must be smaller than this beneath Southeast Greenland in order to explain observed uplift rates there. Finally, Khan et al[3]. also noted the importance of a regional-scale low-viscosity region beneath Southeast Greenland to explain observations of rapid uplift there, but used a GIA modelling approach based on discretized ice loads sitting above different 1D layered Earth models for each drainage basin. This approach is computationally efficient, but has to be used with caution because the lateral extent of the low-viscosity region may be restricted (e.g., in the case of a plume track), reducing modeled uplift rates[18]. The regional-scale models presented here provide a computationally-manageable way to accurately model the impact of 3D rheological complexity on ground uplift rates induced by deglaciation.

Inland extent of the plume-weakened region

While our estimations of the north-south extent of the weakened region are based on observations of uplift along the Southeast Greenland coast, we lack such constraints from Greenland's interior. Thus, the westward (inland) extent of the plume-weakened region remains uncertain. Geophysical observations can provide some constraints: Seismic studies show slow velocity anomalies penetrating into Central Greenland[14,16], but with velocity contrasts that are smaller than observed along the coast[12]. Geothermal heat flux observations[9,45,46] and modelling[11] suggest that the Iceland plume may have weakened the lithosphere of interior Greenland, but substantially

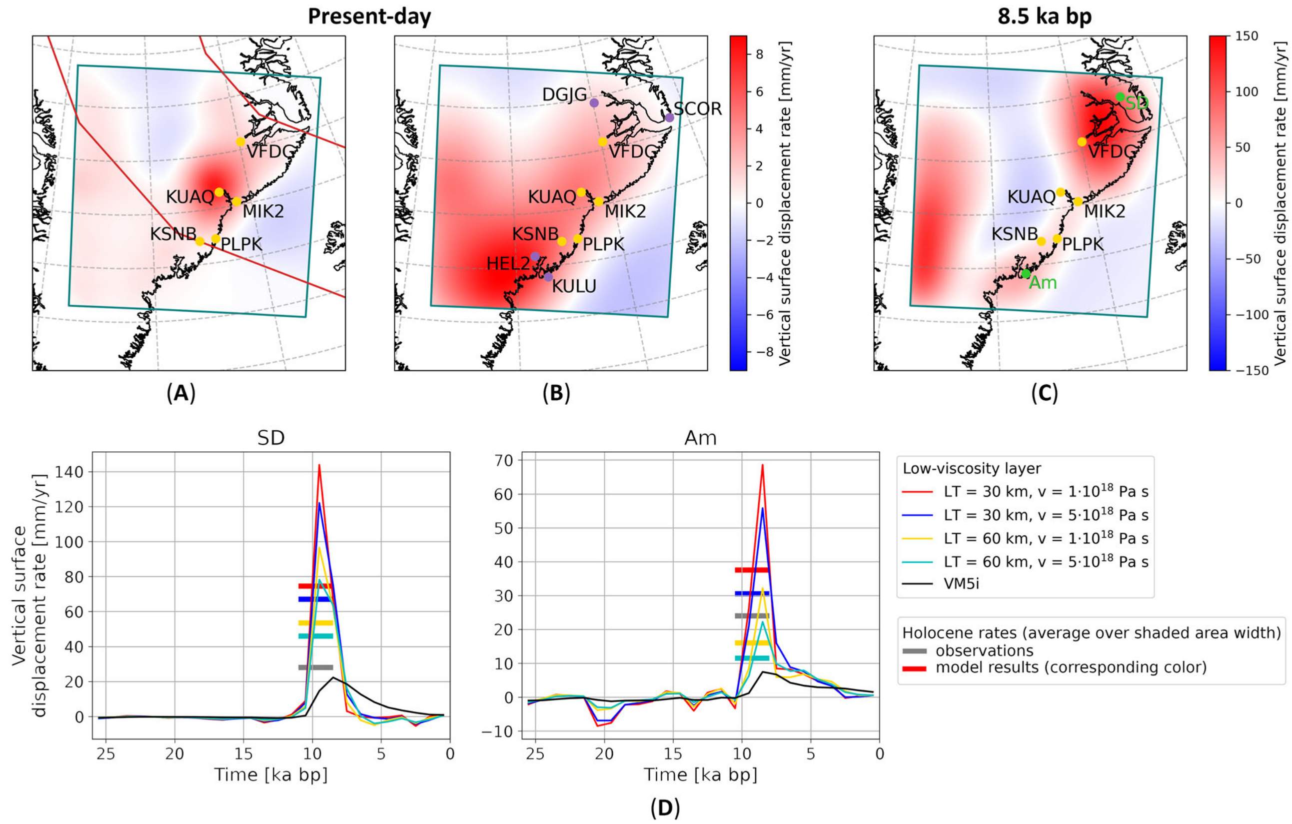

Fig. 7 | Present-day and last deglaciation uplift rates are affected by the horizontal extent of a low-viscosity area. Here we compare models (**A**) for a 600 km wide plume track and (**B**) for a low-viscosity layer that extends across the model domain, including beneath the Helheim glacier, with GNSS stations (yellow and purple dots). These models use a plume track/layer viscosity of $1 \cdot 10^{18}$ Pa s and an effective lithospheric thickness of 45 km (60 km outside the plume track). **C** Uplift rates at 8.5 ka bp for a layer viscosity of $5 \cdot 10^{18}$ Pa s and an effective lithospheric thickness of 22.5 km, with Holocene sea level sites (green). **D** Uplift rates over the last deglaciation for the two sea level sites (SD and Am) for the layered VM5i rheological model (black), observed Holocene uplift (grey bar) and for different layered model results (colored lines and bars).

depend on a single controversial heat flow observation at NGRIP (North GReenland Ice core Project)[45]. Other geophysical constraints from gravity and magnetics suggest only moderate lithospheric thinning in central Greenland between cratonic blocks, but confirm the presence of thin lithosphere along the southeast coast[47]. Our results are consistent with weakening instilled by the Iceland plume along the coast, and are not dependent on a similar weak Earth structure extending into Greenland's interior. This is because uplift rates are most sensitive to local asthenospheric viscosities[18], although nearby weak asthenosphere can moderately affect uplift rates (e.g., Fig. 7A, B). Thus, our modelling provides improved constraints on the Earth structure along the southeast coastal margin, but not the interior of Greenland. Our regional models represent an improvement, but emphasize the need for better geophysical constraints on the heterogeneous viscosity structure beneath Greenland.

Complex rheologies

We employ a Maxwell (linear) viscoelastic rheology and do not explore more complex rheologies such as composite flow laws[48] or time- and stress-dependent viscosity (i.e., transient rheology), which may play an important role on GIA timescales[49–53]. Such rheologies result in different estimates of effective mantle viscosity and lithospheric thickness based on different timescales of deformation. For example, Paxman et al.[52] used a sophisticated rheological calculator, constrained by laboratory deformation studies, to estimate effective viscosities less than 10^{19} Pa s beneath most of Greenland for decadal timescales, and increasing viscosities for longer timescales. By contrast, Pan et al.[33] showed using 1D models with linear viscosity that a moderate low-viscosity layer beneath Greenland's lithosphere can reconcile uplift rates inferred for the millennial timescales of Holocene relative sea level fall with those occurring on the more recent decadal timescales of GNSS observations. Our results similarly employ a classical linear Maxwell viscoelastic rheology law to successfully predict observed rates of early Holocene and modern uplift rates in Southeast Greenland. However, rates of Greenlandic mass loss across millennia in the early Holocene were similar to recent melting rates occurring over the past two decades[54]. Thus, it may be difficult to use a Holocene-to-modern comparison to constrain the potential impact of deglaciation rate on asthenospheric rheology.

Viscous response of the solid Earth to recent ice mass changes

We have shown here that recent ice mass loss, particularly changes during the second millennium and the satellite altimetry era, can drive a rapid viscous response that dominates uplift rates in some parts of Greenland. Previously, it was thought that present-day uplift is controlled by a viscous response to deglaciation during the last glacial cycle (there is no elastic response if ice heights remain constant over the past 2 ka, Fig. S5) and an elastic response to contemporary ice loading changes (the viscous response is slow if mantle viscosity is large)[55]. Although these components contribute to uplift, we find that the viscous response to short-term deglaciation is the largest contributor to uplift above a low-viscosity plume track in Southeast Greenland (Fig. 6). This finding has implications for the interpretation of GNSS uplift rates near areas of past and current (de)glaciation, as has been suggested for Alaska, Patagonia, and the Antarctic Peninsula[56–58]. When correcting observed GNSS uplift rates for elastic deformation due to contemporary ice melt, the remaining signal cannot solely be attributed to ice loading changes over the last glacial cycle in areas of low-viscosity mantle, also because ice mass changes from the second millennium are crucial to include[6]. Instead, more complex 3D modelling, as presented here, is needed near areas of extensive recent deglaciation occurring above low-viscosity mantle[20]. Such modelling is important to accurately infer Earth structure and loading history from uplift observations.

Importance of rapid uplift for future deglaciation

Although present-day uplift rates in Southeast Greenland are mostly insensitive to the plume track characteristics for deglaciation during the last glacial cycle (Fig. S2), our models predict large variations in uplift rates during past time periods with large ice loading changes, particularly between 11 and 8 ka bp (Figs. 2, S3, S4, S16, and S17). The location of GNSS site VFDG is especially sensitive to the choice of Earth model, reaching over 60 mm/yr at around 9 ka bp for a wide plume track (Fig. 2A), a low plume track viscosity (Fig. S3A), or a thin lithosphere (Fig. S4A), and even faster uplift if the weakened Earth region extends further north (Figs. S16, S17). Similarly, rapid uplift at Holocene sea level sites SD and Am likely resulted from a weakened Earth structure (Fig. 7), and manifested as rapid sea level drop (Figs. S15, 7D).

Such large uplift rates during the last deglaciation can have implications for local glacier dynamics on the periphery of the ice sheet, and thus may be important for ice sheet evolution and stability. For instance, we note that tidewater (i.e., marine-terminating) glaciers are the dominant type of outlet glacier in eastern Greenland. Among these, the Kangerlussuaq glacier is characterized by a reverse bed slope[59,60] that can facilitate runaway retreat. However, if the bedrock beneath a tidewater glacier is uplifted quickly, relative sea level falls and the grounding line can advance, stabilizing the glacier[61,62]. This is the case for the Thwaites glacier in West Antarctica, where the uplift from low-viscosity mantle can inhibit marine ice sheet instability, potentially reducing ice mass loss by over 20% after ~100 years[63]. Such feedback between glacier dynamics and solid Earth uplift has not yet been identified for Greenland[54]. However, given that our models predict large uplift rates (up to ~60 mm/yr or more) during periods of rapid ice mass loss in the past (e.g., Fig. 2), models of future deglaciation should consider the impact of rapid ground uplift immediately following deglaciation of Southeast Greenland. Recently, the Kangerlussuaq glacier has experienced substantial thinning and retreat (~200 m over 10 years)[60] and a 9 km retreat earlier in 20th century after the collapse of a large ice tongue (i.e., floating section)[64]. Such large rates of ice mass loss, sitting above the weakened viscosities (possibly as low as ~10^{18} Pa s) of the Iceland plume track, are driving rapid ground uplift with potentially important implications for both grounding line movement and glacier stability[1].

Methods

GIA modelling approach

We perform regional modelling across Southeast Greenland, because shallow and confined local viscosity variations only affect uplift rates locally[18]. We choose the model domain, ice loading area, and area of interest (boxes in Fig. 1A) so as to minimize the influence of external ice loads and the regional model's lateral boundaries on solid Earth deformation within our area of interest. We impose a plume track[9] (Fig. 1B, black line) with varying widths W_{PT} (200, 400, or 600 km) (Fig. 1B, C) within an otherwise radially symmetric rheological model VM5i (Table S3) with a chosen lithospheric thickness T_{LT} (30, 60, or 90 km). Inside this track, we implement low mantle viscosity η_{PT} ($1 \cdot 10^{18}$, $5 \cdot 10^{18}$, $1 \cdot 10^{19}$, or $5 \cdot 10^{19}$ Pa s) and a lithosphere that is thinned by Δh (25% of T_{LT}, see below)[11] (Fig. 1C). We vary these Earth model parameters within a plausible range, based on observations and modelling studies (see below), because they are not well constrained and can greatly affect solid Earth deformation rates[18].

For high-resolution regional modelling that includes a low-viscosity plume track, we impose ice loading changes over three different time periods: the satellite altimetry era (1992–2020 AD), the second millennium (1000–1995 AD), and the last glacial cycle (since 122 ka bp). For contemporary ice load changes, we make use of a 1992–2020 record of Greenland ice sheet altimetric/volume-derived mass balance (VMB) obtained from multisatellite Ku-band altimetry[30] (Fig. 1A, B). For the second millennium we use a Bayesian estimate of ice mass change[6] (Fig. S18) for the Little Ice Age, with maximum glacial extents during 1400–1900, consistent with ice core constraints on cooling during this period[65]. We apply spatial variations with the same patterns as for the contemporary ice load changes. For the last glacial cycle, we use the ICE-6G_C(VM5a) ice history model[21,29] (Fig. S5).

Ice mass changes outside of our ice loading area can affect recent vertical motion in Southeast Greenland in two ways. First, due to its location on the collapsing peripheral bulge of the former Laurentide ice sheet over North America, most of Greenland is experiencing subsidence resulting from past deglaciation of the Laurentide ice sheet[21,29]. Second, recent deglaciation occurring elsewhere in Greenland (outside the ice loading area) induces a long-wavelength elastic response that dominantly uplifts Greenland. We model these two contributions (see below for details on the modelling codes, Earth structure, and ice loading). The total modeled deformation rates within our region of interest thus consist of a summation of five rates: three from regional solid Earth deformation modelling and two from global models of Earth deformation resulting from deglaciation occurring outside our ice loading area.

Regional models: viscoelastic deformation driven by deglaciation of Southeast Greenland

For regional-scale loads (those within the ice loading area), we use ASPECT (Advanced Solver for Problems in Earth's ConvecTion) v2.4.0[23–27] to model viscoelastic solid Earth deformation in Southeast Greenland. ASPECT is a finite element open-source code (see Code availability statement), originally built for solid Earth thermal convection studies, that can be used to model solid Earth deformation and that is optimized for handling lateral variations in Earth material properties. We use a 3D box model geometry with a free surface on the top boundary[27], allowing for mesh deformation, and free-slip boundary conditions (i.e., only boundary-parallel flow) on the bottom and lateral boundaries. This setup allows us to accurately predict vertical[28] but not horizontal[27] motions of the free surface in response to imposed surface tractions. The incompressible viscoelastic rheology is modeled according to Moresi et al.[66], as outlined in Sandiford et al.[67]. Although regional modelling in ASPECT can include a variety of viscoelastic-plastic rheologies (e.g., dislocation creep, diffusion creep or composite viscous flow laws), solutions using non-linear rheologies have not been benchmarked yet in combination with a free surface and boundary traction. Such benchmark tests have also not yet included compressibility, despite its potential importance for horizontal surface displacements[68,69]. Our model setup with a free surface, incompressibility, Maxwell viscoelastic rheology, and boundary traction, is benchmarked for glacial cycle and contemporary ice loading timescales[28].

We model ice loading changes over an area of 1000 km by 1000 km with corners at (73.49°N, 48.96°W), (71.69°N, 18.89°W), (63.38°N, 27.52°W), and (64.53°N, 47.54°W) (Fig. 1A, teal box). Our area of interest lies within the ice loading area, 250 km away from the boundaries of the ice loading area, which reduces the effect of ice loading changes outside the ice loading area on solid Earth deformation within the area of interest (Fig. 1A, blue box). A border of 500 km is added beyond the ice loading area in each direction to reduce the effect of the model's lateral boundaries (edge effects associated with the model) on solid Earth deformation within the area of interest (Fig. 1A, pink box). Because we omit ice loads within this border region, we can utilize decreased resolution in this region for increased computational efficiency, while still resolving deformation within our area of interest. This is possible because deformation within the low-viscosity plume track is rather localized (e.g., Fig. 3). Deformation caused by ice loading occurring outside the ice loading area (including within the border region) is modelled using global models (see below). The horizontal box dimensions are thus 2000 km by 2000 km. The depth of the model is 2891 km to the core-mantle boundary (Table S3). The mesh resolution within the ice loading area is 6.25 km horizontally and 6.02 km vertically, down to 120 km depth. Outside the high-resolution volume, the mesh resolution below 1000 km depth is 100 km horizontally and 96.37 km vertically, and it is 50 km horizontally and 48.18 km vertically everywhere else[28].

To construct regional models of solid Earth deformation due to glacial cycle ice loading (since 122 ka bp), we interpolate the ICE-6G_C ice history data onto a 5 km grid (same as VMB data grid) within our ice loading area (ice loading inputs are discussed in a later subsection). If we apply the same VM5i rheology model (Table S3) as for the global models (Fig. S5), we find that vertical surface displacement rates in the ice loading area are similar for both global and regional modelling approaches (Fig. S1B). Differences are <0.05 mm/yr at KUAQ, MIK2, KSNB, and PLPK and 0.38 mm/yr at VFDG (Table S1), which are well within the uncertainty of the GNSS uplift observations (Fig. S19). This shows that the effects of sea level change and rotational feedback, which are included in global models but not in our regional modelling, are relatively small for models on this regional scale. Furthermore, differences away from the stations are <1.4 mm/yr (Fig. S1B), which is generally smaller than the uplift differences between Earth models with different track parameters (Fig. 4). This comparison shows that edge effects inherent to the regional models are minimal within the area of interest, and validates our use of a regional modelling approach.

Global models: viscoelastic deformation driven by deglaciation outside of Southeast Greenland

The above-described regional models cannot compute solid Earth deformation due to loads positioned outside the ice loading area (Fig. 1A, teal box). Of these loads, only last glacial cycle loading has a sufficiently long timescale such that far-field loads can drive local ground motion via viscous deformation of the sub-asthenospheric mantle[33]. We compute this deformation using global viscoelastic models, as described below. Because second millennium and satellite altimetry era loads are more recent, they have only had time to drive sizable deformation within the low-viscosity asthenosphere, and thus they can produce ground motion only locally[33]. Thus, we can ignore the viscous contribution from far-field loading at these timescales. We do, however, compute Earth's elastic response to satellite era deglaciation across Greenland, because this deformation occurs instantaneously and has a long-wavelength component that contributes to the GNSS observations.

Due to Greenland's location on the peripheral bulge of the former Laurentide ice sheet, Greenland is still experiencing subsidence following the deglaciation of that ice sheet. To compute vertical motions within Southeast Greenland due to these far-field loads, we perform global solid Earth deformation modelling using SELEN (Sea lEveL EquatioN solver) v4.0[70], which is a pseudo-spectral open-source code that simulates GIA processes (solid Earth deformation and the gravitationally-consistent redistribution of ocean water) occurring in response to the melting of the Late Pleistocene ice sheets. This model is built for radially symmetric Earth models, and includes shoreline migration and rotational feedback. We use SELEN to capture the subsidence and uplift in Southeast Greenland that results from global ice and ocean mass changes occurring outside of the ice loading area (Fig. 1A, teal box) during the last glacial cycle. The solid Earth response to ice inside this ice loading area is handled by regional models (see above). Because the implementation of loads within SELEN is done in the spectral domain, there may be some leakage of loading from outside to inside the ice loading area. However, the total loading across the region remains unchanged by the split between separate modelling techniques (ASPECT and SELEN), and our use of a maximum harmonic degree of 128 in the SELEN models (corresponding to half wavelengths of ~150 km) means that the inward leakage of loading should be limited to a fraction of this length scale. Any leakage should therefore not affect our area of interest (blue box, Fig. 1A), which lies 250 km from the edge of the ice loading area.

Our global GIA modelling with SELEN predicts large uplift over North America resulting from deglaciation of the Laurentide ice sheet, over Scandinavia due to melting of the Fennoscandian ice sheet, and over (West) Antarctica (Fig. S20A). We observe a small degree 2 signal related to the rotational feedback[71,72]. Even though the mass of the Greenland ice sheet has been greatly reduced since the last glacial maximum (Fig. S5A within ice loading area), we observe subsidence across most of Greenland (Fig. S20B). This is due to Greenland's location on the collapsing peripheral bulge of the former Laurentide ice sheet over North America. Uplift does occur in northern Greenland, due to its greater distance to the Laurentide ice sheet and its larger mass loss since 4 ka bp compared to the rest of Greenland (Fig. S5). Ice loading outside of our ice loading area drives subsidence across Southeast Greenland (Fig. S20C), with negative vertical displacement rates at our GNSS sites of a few mm/yr (Table S2.i). Ice unloading occurring inside the ice loading area drives uplift (Fig. S20D), consistent with our regional modelling (Fig. S1). This signal is already included within the high-resolution regional models (Fig. S2), and therefore we exclude it from the global models. Subsidence west of the model domain (Fig. S20D) is caused by the ice mass gain from 4 to 2 ka bp (Fig. S5B).

We have used SELEN to validate the usability of ASPECT for regional solid Earth deformation modelling for glacial cycle ice loading changes. To do this, we compute solid Earth deformation following ice loading changes over the last glacial cycle for ice within the ice loading area in Southeast Greenland only (Fig. 1A, teal box only), using both the SELEN model and an ASPECT model with the same viscosity structure (Fig. S1). For the SELEN models, we use a Tegmark grid resolution of 44 (equating to a 0.42° radius of disks on a sphere), a maximum harmonic degree of 128, the revised rotational theory[71,72], and 3 internal and external iterations of the sea level equation (see Spada et al.[70] for details). The similarity of the deformation predicted by both models (Fig. S1B) indicates that (i) leakage of loads across the edges of the ice loading area does not substantially affect deformation patterns within the area of interest, and (ii) the regional ASPECT model captures broad-scale deformation patterns that are consistent with those computed by global models (e.g., SELEN).

Recent deglaciation of Greenland occurring outside our ice loading area can generate long-wavelength elastic deformation that contributes to vertical motion[73] of Southeast Greenland. For this elastic component, we compute deflections of the solid Earth and sea surfaces resulting from Earth's elastic response to recent (2009–2020, chosen to overlap with the GNSS observations, see below) ice loading changes over Greenland (excluding the ice loading area, Fig. 1A, teal box). Elastic deformation is computed following Farrell's[74] Green's function approach, as implemented by Conrad and Hager[73] (not including rotational feedback, but including the degree 1 movement of Earth's center of mass, which amounts to less than 0.2 mm/yr at the GNSS sites). Overall, this elastic contribution, which captures Earth's long-wavelength elastic response, has only a small effect within the ice loading area (Figs. 3E and S21A) because the elastic response to loading is rather local. Uplift rates decrease eastward, because of increasing distance to the nearest major ice loading area in western Greenland, and are smaller than 1 mm/yr at the five GNSS sites (Table S2.ii).

Earth structure and variations

For the simulations in SELEN, we use the radially symmetric 11-layer VM5i rheology model (Table S3)[70], which is an adaption to the VM5a model[21,29] without elastic compressibility, with a lower mantle viscosity ranging between $1.5\text{-}3.2 \cdot 10^{21}$ Pa s from 670 km depth to the core-mantle boundary. In ASPECT we also use the VM5i rheological model, excluding the core and with constant volume-averaged mantle density of 4423.61 kg/m^3 [28]. For the regional models in ASPECT, we apply a plume track to the VM5i model that extends from the bottom of the upper mantle layer UM1 to the bottom of the lithosphere. Above the plume track the lithosphere is thinned by Δh, which describes lithospheric thinning due to passage of Greenland over the Iceland plume. This lithospheric thinning is set to 25% of the surrounding lithospheric thickness (Fig. 1C), which is consistent with models of thermal ablation by plume-lithosphere interaction[11] and indications from seismic tomography[12,14–16]. We vary the lithospheric thickness, plume track width, and plume track viscosity, and test for all possible combinations. The lithospheric thickness outside the track varies between 30, 60, and 90 km (thereby changing the thickness of upper mantle layer UM1), which is within the plausible range of elastic lithospheric thicknesses in Greenland[13,15,75]. We employ plume track widths of 200, 400, and 600 km and a plume track trajectory following Martos et al.[9]. The plume track width is not well constrained, and model choices are based on findings from seismics and magnetics (geothermal heat flow)[10,12,14–16]. The plume track lies within the upper mantle layer, which has a viscosity of $5 \cdot 10^{20}$ Pa s (Table S3), consistent with different ice sheet deglaciation studies[21,29,37]. We vary the viscosity of the plume track across a range of low viscosities of $1 \cdot 10^{18}$, $5 \cdot 10^{18}$, $1 \cdot 10^{19}$, and $5 \cdot 10^{19}$ Pa s. For the low-viscosity layer case, the plume track is set to occupy the entire regional model domain, and thus the entire lithosphere is thinned by 25% from nominal values (to 22.5, 45, or 67.5 km).

Ice loading changes for model input

We model solid Earth deformation in response to ice loading changes over three different periods: the satellite altimetry era (1992–2020 AD), the second millennium (1000–1995 AD), and the last glacial cycle (since 122 ka bp). For contemporary ice load changes, we make use of a 1992–2020 record of Greenland ice sheet altimetric/volume-derived mass balance (VMB) derived from multisatellite Ku-band altimetry[30]. This 5 km resolution dataset combines altimetry observations from the ERS-1, ERS-2, ENVISAT, Cryosat-2, and Sentinel-3A satellites, and accounts for changes in radar penetration depths, elevation dependent near-surface density, and vertical solid Earth deformation in the conversion from elevation change to mass balance. This dataset shows mass balances comparable to mass balance ranges compiled from other methods such as satellite gravimetry and the input-output method, and other satellite altimetry datasets[35]. The advantage of using satellite altimetry rather than gravimetry to estimate mass change is its higher resolution, which is important for regional modelling. Also, estimates based on satellite altimetry are less affected by solid Earth deformation[76]. Solid Earth uplift rates in Greenland are on the order of millimeters[3] whilst the surface elevation change from altimetry is much larger, on the order of meters[35,77]. Note that the GIA corrections applied to ice surface height changes from satellite altimetry do not include viscous deformation on short timescales, which we show can be important above areas of low-viscosity mantle. This may introduce an error in ice volume changes estimates of a few percent[78], thereby affecting predicted uplift rates. We convert the altimetry-derived constraints on annual mass change per unit area into pressure change using a surface gravity of 9.81 m/s^2 and 25 km^2 cell areas. The pressure change is applied as a boundary traction to the top boundary in ASPECT, with a time step size of 1 yr. These altimetry-derived ice mass changes are also used to compute the elastic response to recent ice loading changes over Greenland (excluding ice in the previously defined ice loading area, denoted by the teal box in Fig. 1A). For these elastic calculations (see above), we use the temporal average mass change over the period of GNSS observations (2009-2020, see next section on GNSS uplift rates).

Adhikari et al.[6] found that including an estimate of the ice loading change since 1000 AD greatly improved the fit between modeled and observed uplift rates at GNSS stations across Greenland. However, Adhikari et al.[6] excluded from their analysis GNSS stations in Southeast Greenland, because these sites are possibly affected by the Iceland plume. Here we use the estimated total mass anomaly across Greenland, as given by Fig. 2a of Adhikari et al.[6], and scale it by the fraction of Greenland's recent mass change (from the VMB data) occurring within the ice loading area (this fraction is 0.40). We assign a spatial pattern for second millennium mass changes that follows the average ice loading changes from the VMB data (Fig. 1A, B). The reference mass anomaly at year 1000 is zero and is zero again at year 1995 (Fig. S18), and thus there is no net change is mass across the second millennium. This means that there is only a viscous and no elastic response to second millennium loading at the present-day. We apply loads consistent with these ice changes from the year 1000 to 1995, and then let the ASPECT model run for another 25 years with zero loading, until 2020, to find the solid Earth deformation due to relaxation after second millennium ice loading. Time step sizes for the input data and the deformation model are 5 yr.

The third period of interest is the last glacial cycle (since 122 ka bp). We use the ICE-6G_C(VM5a) ice history model[21,29] on a 1° by 1° global grid. In SELEN we apply all ice loading changes outside of the Southeast Greenland ice loading area (Fig. 1A, teal box), to compute the subsidence of Southeast Greenland as a consequence of global ice and ocean mass changes over the last glacial cycle. We also run SELEN using only ice loading changes in the Southeast Greenland ice loading change area in order to validate the usability of ASPECT for regional solid Earth deformation modelling due to glacial cycle ice loading changes (Fig. S1). For the regional models in ASPECT we interpolate the ICE-6G_C ice heights to the 5 km VMB grid in space and to 500 yr intervals in time, for model runs in ASPECT with a 100 yr numerical time step size. The ice loading changes are zero from 2 ka bp onwards (Fig. S5).

The choice of numerical time step size in ASPECT for the three glacial loading periods is based on the timescale for solid Earth deformation output. Tests show that smaller time step sizes than ones used here produce nearly identical output. Furthermore, uncertainties in the ice loading input are larger than any small deviation introduced by the choice of numerical time step size (e.g., see Fig. 2a of Adhikari et al.[6] for the large uncertainties associated with second millennium ice loading).

GNSS uplift rates

We obtain processed (i.e. data product level 2) GNSS station height information from the Greenland GNSS Network (GNET) from the stations Kangerdlussuaq Gletscher (KUAQ)[79], Mikis Fjord (MIK2)[80], Pilappik (PLPK)[81], Steenstrup Nordre Bræ (KSNB)[82], and Vestfjord Gletscher (VFDG)[83] (Figs. 1B, S19), as well as Daugaard Jensen Gletscher (DGJG)[84], Scoresbysund (SCOR)[85], Helheim Glacier (HEL2)[86], and Kulusuk (KULU)[87] (Figs. 7B, S22). This data is openly available through the GAGE Facility, operated by UNAVCO (see Data availability statement). We compute linear regression trends and the standard deviation of the detrended data at these nine stations for the period from the start of observations to the end of the VMB data at 31-12-2019 (Fig. S19). The start of observations is 7-8-2009 for KUAQ, 8-8-2009 for MIK2, 12-8-2007 for PLPK, 21-8-2007 for KSNB, 9-8-2009 for VFDG, 12-08-2009 for DGJG, 02-02-2005 for SCOR, 25-08-2007 for HEL2, and 25-07-1996 for KULU. To determine trends over similar time periods, SCOR and DGJG are processed starting 12-08-2009, and KULU and HEL2 starting 25-08-2007.

To estimate uplift rates and standard deviations, we perform linear regression analysis over the period of observations (Figs. S19, S22, and Table S2.vi). The largest uplift rate of 17.44 ± 1.10 mm/yr occurs at KUAQ, which lies near the outlet of the Kangerlussuaq glacier, one of Greenland's fastest mass-losing glaciers[38,60]. Nearby MIK2 also shows rapid uplift of 12.39 ± 0.83 mm/yr. To the north, station VFDG shows a smaller uplift rate of 4.95 ± 0.73 mm/yr. PLPK and KSNB to the south are located close to the Helheim glacier, also one of Greenland's three largest glaciers based on catchment size, and also deglaciating rapidly[38], show rapid uplift at 9.70 ± 0.82 mm/yr and 12.85 ± 0.68 mm/yr, respectively. Four additional stations are located inside our ice loading area but outside our area of interest (Fig. 7B). These are DGJG[84] and SCOR[85] to the north, with slower uplift rates of 3.75 ± 0.81 and 2.07 ± 0.68 mm/yr, respectively, and HEL2[86] and KULU[87] to the south with rapid uplift rates of 15.93 ± 0.78 and 8.54 ± 0.56 mm/yr, respectively (Fig. S22). DGJG and HEL2 sit close to the present-day ice margin, whereas SCOR and KULU are currently far from the present-day ice margin, but were closer to it during the last deglaciation.

We compare uplift rates for the five primary GNSS stations (Fig. S19) to model predictions from the combination of global and regional deformation modelling (see above). Because the solid Earth deformation models are driven by ice loading changes operating on different timescales (satellite altimetry era, the second millennium, and the last glacial cycle), we measure average vertical displacement rates from the models also using different timescales. For deformation due to satellite altimetry era modelling, we measure from 2009 (or 2007 for PLPK and KSNB) to 2020 (numerical time step size of 1 yr). For the second millennium, we measure from 2010 to 2020 (numerical time step size of 5 yr). For the last glacial cycle, we measure from 1920 to 2020 (numerical time step size of 100 yr). Although 100 yr seems like a large time step for determining uplift rates to compare to GNSS observations (2007/2009 to 2020), we note that ice heights in Southeast Greenland remained nearly constant from 4 ka bp to present day in the ICE-6G_C model (Fig. S5). Thus, present-day uplift rates from the last glacial cycle reflect the Earth's continued response to deglaciation that ended several millennia ago, and thus have remained nearly constant during in the past century.

Holocene uplift rates

Relative sea level (RSL) estimates are scarce along the southeast coast of Greenland. We use geologic indicators of RSL to constrain uplift rates over the Holocene at two sites: Schuchert Dal (SD)[31] and Ammassalik (Am)[32] in the northern and southern parts of our ice loading area, respectively (Figs. 1B and 7C). Rapid relative sea level drop, consistent with ground uplift, is observed in both locations in the Early Holocene during and following Greenland deglaciation (Fig. S15). For Ammassalik, Long et al.[32] compiled RSL estimates based on sediment cores from isolation and lake basins (4 RSL estimates from lakes below the marine limit, 2 upper RSL bounds from lakes above the marine limit) and determined a local marine limit of 69 m at around 11 ka bp from the lower limit of perched boulders above wave-washed bedrock. From these RSL estimates we estimate a land uplift rate of 24 mm/yr during 10.5 and 8.0 ka bp (Fig. S15A). For Schuchert Dal, Hall et al.[31] compiled RSL estimates based on field mapping of surficial deposits (shells) and examination of landforms (stratigraphic sections exposed in stream cuts). There are 62 samples of RSL estimates and another 34 with less confidence in water levels (e.g., from fjord samples) providing lower bounds on RSL. From these RSL estimates we estimate a land uplift rate of 28 mm/yr during 11.0 and 8.5 ka bp (Fig. S15B).

We relate our model predictions of uplift rate to RSL observations (Figs. 2B, 7D, S3B, and S4B). In doing so, we assume that the observed RSL drop is dominated by bedrock uplift driven by nearby deglaciation. This assumption may be violated in several ways. First, loss of local ice mass loss in Greenland would lower RSL around Greenland due to reduced gravitational attraction of seawater to the ice sheet. Indeed, Greenland lost an ice volume equivalent to 2–3 meters of sea level during 11–8 ka bp[88], which, if distributed around Greenland's periphery, would have resulted in an approximately equivalent depression of the geoid around Greenland[73]. Although the geoid depression may have been larger near areas of more concentrated mass loss, the associated sea level drop (~ 1 mm/yr) only explains a small part of the 60–70 m that is observed (Fig. S15). Second, uplift or subsidence may be driven by ice loading changes outside of our ice loading area. In particular, the collapse of the peripheral bulge to the North America Ice Complex led to subsidence across much of Greenland[37]. However, our global modelling in SELEN (e.g., to compute Fig. 3D) suggests that this mechanism contributes only ~3.3 mm/yr of subsidence along the Southeast Greenland coast during the early Holocene, mostly driven by North American melt occurring prior to 11 ka bp. Third, eustatic sea level rose by ~25 meters during 11–8 ka bp[21], mostly due to ice melting outside of Greenland. Based on normalized sea level fingerprints[89] and ice volume changes[90,91] we estimate that the Southeast Greenland coast only experienced RSL rise of 7.8 m during 11–8 ka bp, or ~2.6 mm/yr, due to melting of non-Greenlandic ice. In this estimate we exclude Greenlandic ice loss (it is included separately as described above), Laurentide and Antarctic ice contribute 6.0 m and 1.8 m of RSL respectively, and the fingerprint of Fennoscandian ice melt shows a minimal RSL effect in Southeast Greenland[89]. The sum of the three processes described above, together indicating about 5 mm/yr of RSL rise, is uncertain but small compared to the observed sea level drop (Fig. S15) and of opposite sign. Thus, the Holocene land uplift that we estimate for SD and Am (Fig. S15) likely represents a lower bound.

Data availability

The Greenland VMB data is available on the database of the Technical University of Denmark, DTU Data (https://data.dtu.dk/articles/dataset/Greenland_Ice_Sheet_mass_balance_1992-2020_from_calibrated_radar_altimetry/13353062). The ICE-6G_C(VM5a) ice history model is available via the University of Toronto (https://www.atmosp.physics.utoronto.ca/~peltier/data.php). The GNSS station positions are available via the GAGE Facility (https://www.unavco.org/instrumentation/networks/status/polenet#gnet and https://data.unavco.org/).

Code availability

The open-source code ASPECT (v2.4.0)[23–27] is available for download on GitHub (https://github.com/geodynamics/aspect/releases/tag/v2.4.0) or Zenodo (https://doi.org/10.5281/zenodo.6903424). The open-source code SELEN v4.0[70] is available for download on Zenodo (https://doi.org/10.5281/zenodo.3520451). ASPECT parameter and log files and SELEN configuration and ice input files for the simulations in this study are available for download on Zenodo (https://doi.org/10.5281/zenodo.8192717).

Received: 10 May 2024; Accepted: 16 December 2024;
Published online: 26 December 2024

References

1. Whitehouse, P. L. Glacial isostatic adjustment modelling: historical perspectives, recent advances and future directions. *Earth Surf. Dyn.* **6**, 401–429 (2018).
2. Simpson, M. J. R., Wake, L., Milne, G. A. & Huybrechts, P. The influence of decadal- to millennial-scale ice mass changes on present-day vertical land motion in Greenland: Implications for the interpretation of GPS observations. *J Geophys Res. Solid Earth* **116**, B02406 (2011).
3. Khan, S. A. et al. Geodetic measurements reveal similarities between post–Last Glacial Maximum and present-day mass loss from the Greenland ice sheet. *Sci. Adv.* **2**, e1600931 (2016).
4. Bevis, M., Wahr, J., Khan, S. A. & Francis, O. Bedrock displacements in Greenland manifest ice mass variations, climate cycles and climate change. *Proc. Natl. Acad. Sci.* **2012**, 11944–11948 (2012).
5. Milne, G. A. et al. The influence of lateral Earth structure on glacial isostatic adjustment in Greenland. *Geophys. J. Int.* **214**, 1252–1266 (2018).
6. Adhikari, S. et al. Decadal to centennial timescale mantle viscosity inferred from modern crustal uplift rates in Greenland. *Geophys. Res. Lett.* **48**, e2021GL094040 (2021).
7. Steinberger, B., Bredow, E., Lebedev, S., Schaeffer, A. & Torsvik, T. H. Widespread volcanism in the Greenland–North Atlantic region explained by the Iceland plume. *Nat. Geosci.* **12**, 61–68 (2019).
8. Forsyth, D. A., Morel-A-L'Huissier, I., Asudeh, I. & Green, A. G. Alpha Ridge and iceland-products of the same plume? *J. Geodyn.* **6**, 197–214 (1986).
9. Martos, Y. M. et al. Geothermal heat flux reveals the Iceland hotspot track underneath Greenland. *Geophys. Res. Lett.* **45**, 8214–8222 (2018).
10. Rogozhina, I. et al. Melting at the base of the Greenland ice sheet explained by Iceland hotspot history. *Nat. Geosci.* **9**, 366–369 (2016).
11. Heyn, B. H. & Conrad, C. P. On the relation between basal erosion of the lithosphere and surface heat flux for continental plume tracks. *Geophys. Res. Lett.* **49**, e2022GL098003 (2022).
12. Mordret, A. Uncovering the Iceland hot spot track beneath Greenland. *J. Geophys. Res. Solid Earth* **123**, 4922–4941 (2018).
13. Steffen, R., Audet, P. & Lund, B. Weakened lithosphere beneath Greenland inferred from effective elastic thickness: a hot spot effect? *Geophys. Res. Lett.* **45**, 4733–4742 (2018).
14. Celli, N. L., Lebedev, S., Schaeffer, A. J. & Gaina, C. The tilted Iceland Plume and its effect on the North Atlantic evolution and magmatism. *Earth Planet. Sci. Lett.* **569**, 117048 (2021).
15. Pourpoint, M., Anandakrishnan, S., Ammon, C. J. & Alley, R. B. Lithospheric structure of Greenland from ambient noise and earthquake surface wave tomography. *J. Geophys. Res. Solid Earth* **123**, 7850–7876 (2018).
16. Antonijevic, S. K. & Lees, J. M. Effects of the Iceland plume on Greenland's lithosphere: new insights from ambient noise tomography. *Polar Sci.* **17**, 75–82 (2018).

17. Fahnestock, M., Abdalati, W., Joughin, I., Brozena, J. & Gogineni, P. High geothermal heat flow, basal melt, and the origin of rapid ice flow in central Greenland. *Science* **294**, 2338–2342 (2001).
18. Weerdesteijn, M. F. M., Conrad, C. P. & Naliboff, J. B. Solid earth uplift due to contemporary ice melt above low-viscosity regions of the upper mantle. *Geophys. Res. Lett.* **49**, e2022GL099731 (2022).
19. Kierulf, H. P. et al. Time-varying uplift in Svalbard—an effect of glacial changes. *Geophys. J. Int.* **231**, 1518–1534 (2022).
20. Nield, G. A. et al. Rapid bedrock uplift in the Antarctic Peninsula explained by viscoelastic response to recent ice unloading. *Earth Planet. Sci. Lett.* **397**, 32–41 (2014).
21. Peltier, W. R., Argus, D. F. & Drummond, R. Space geodesy constrains ice-age terminal deglaciation: the global ICE-6G_C (VM5a) model. *J. Geophys. Res. Solid Earth* **120**, 450–487 (2015).
22. Klemann, V., Ivins, E. R., Martinec, Z. & Wolf, D. Models of active glacial isostasy roofing warm subduction: case of the South Patagonian Ice Field. *J. Geophys. Res. Solid Earth* **112**, B09405 (2007).
23. Kronbichler, M., Heister, T. & Bangerth, W. High accuracy mantle convection simulation through modern numerical methods. *Geophys. J. Int.* **191**, 12–29 (2012).
24. Heister, T., Dannberg, J., Gassmöller, R. & Bangerth, W. High accuracy mantle convection simulation through modern numerical methods – II: realistic models and problems. *Geophys. J. Int.* **210**, 833–851 (2017).
25. Bangerth, W. et al. *ASPECT v2.4.0*, Zenodo https://doi.org/10.5281/zenodo.6903424 (2022).
26. Bangerth, W. et al. *ASPECT: Advanced Solver for Problems in Earth's ConvecTion, User Manual* https://doi.org/10.6084/m9.figshare.4865333 (2022).
27. Rose, I., Buffett, B. & Heister, T. Stability and accuracy of free surface time integration in viscous flows. *Phys. Earth Planet. Inter.* **262**, 90–100 (2017).
28. Weerdesteijn, M. F. M. et al. Modeling viscoelastic solid earth deformation due to ice age and contemporary glacial mass changes in ASPECT. *Geochem. Geophys. Geosyst.* **24**, e2022GC010813 (2023).
29. Argus, D. F., Peltier, W. R., Drummond, R. & Moore, A. W. The Antarctica component of postglacial rebound model ICE-6G_C (VM5a) based upon GPS positioning, exposure age dating of ice thicknesses, and relative sea level histories. *Geophys. J. Int.* **198**, 537–563 (2014).
30. Simonsen, S. B., Barletta, V. R., Colgan, W. T. & Sørensen, L. S. Greenland ice sheet mass balance (1992–2020) from calibrated radar altimetry. *Geophys. Res. Lett.* **48**, e2020GL091216 (2021).
31. Hall, B. L., Baroni, C. & Denton, G. H. Relative sea-level changes, Schuchert Dal, East Greenland, with implications for ice extent in late-glacial and Holocene times. *Quat. Sci. Rev.* **29**, 3370–3378 (2010).
32. Long, A. J. et al. Late Weichselian relative sea-level changes and ice sheet history in southeast Greenland. *Earth Planet. Sci. Lett.* **272**, 8–18 (2008).
33. Pan, L., Mitrovica, J. X., Milne, G. A., Hoggard, M. J. & Woodroffe, S. A. Timescales of glacial isostatic adjustment in Greenland: is transient rheology required? *Geophys. J. Int.* **237**, 989–995 (2024).
34. Greene, C. A., Gardner, A. S., Wood, M. & Cuzzone, J. K. Ubiquitous acceleration in Greenland Ice Sheet calving from 1985 to 2022. *Nature* **625**, 523–528 (2024).
35. The IMBIE Team. Mass balance of the Greenland Ice Sheet from 1992 to 2018. *Nature* **579**, 233–239 (2020).
36. Khan, S. A. et al. Greenland mass trends from airborne and satellite altimetry during 2011–2020. *J. Geophys. Res. Earth Surf.* **127**, e2021JF006505 (2022).
37. Lecavalier, B. S. et al. A model of Greenland ice sheet deglaciation constrained by observations of relative sea level and ice extent. *Quat. Sci. Rev.* **102**, 54–84 (2014).
38. Khan, S. A. et al. Centennial response of Greenland's three largest outlet glaciers. *Nat. Commun.* **11**, 5718 (2020).
39. Steinberger, B., Sutherland, R. & O'Connell, R. J. Prediction of Emperor-Hawaii seamount locations from a revised model of global plate motion and mantle flow. *Nature* **430**, 167–173 (2004).
40. O'Neill, C., Müller, D. & Steinberger, B. On the uncertainties in hot spot reconstructions and the significance of moving hot spot reference frames. *Geochem. Geophys. Geosyst.* **6**, Q04003 (2005).
41. Doubrovine, P. V., Steinberger, B. & Torsvik, T. H. Absolute plate motions in a reference frame defined by moving hot spots in the Pacific, Atlantic, and Indian oceans. *J. Geophys. Res. Solid Earth* **117**, B09101 (2012).
42. Darbyshire, F. A., Dahl-Jensen, T., Larsen, T. B., Voss, P. H. & Joyal, G. Crust and uppermost-mantle structure of Greenland and the Northwest Atlantic from Rayleigh wave group velocity tomography. *Geophys. J. Int.* **212**, 1546–1569 (2018).
43. Fleming, K. & Lambeck, K. Constraints on the Greenland Ice Sheet since the Last Glacial Maximum from sea-level observations and glacial-rebound models. *Quat. Sci. Rev.* **23**, 1053–1077 (2004).
44. Simpson, M. J. R., Milne, G. A., Huybrechts, P. & Long, A. J. Calibrating a glaciological model of the Greenland ice sheet from the Last Glacial Maximum to present-day using field observations of relative sea level and ice extent. *Quat. Sci. Rev.* **28**, 1631–1657 (2009).
45. Colgan, W. et al. Greenland geothermal heat flow database. *Earth Syst. Sci. Data* **14**, 2209–2238 (2022).
46. Conrad, C. P. The solid Earth's influence on sea level. *Geol. Soc. Am. Bull.* **125**, 1027–1052 (2013).
47. Wansing, A., Ebbing, J. & Moorkamp, M. The lithospheric structure of Greenland from a stepwise forward and inverse modelling approach. *Geophys. J. Int.* **238**, 719–741 (2024).
48. Ivins, E. R., van der Wal, W., Wiens, D. A., Lloyd, A. J. & Caron L. Antarctic upper mantle rheology. *Geol. Soc. Lond. Mem.* **56**, 267–294 (2021).
49. Blank, B., Barletta, V., Hu, H., Pappa, F. & van der Wal, W. Effect of lateral and stress-dependent viscosity variations on GIA induced uplift rates in the Amundsen sea embayment. *Geochem. Geophys. Geosyst.* **22**, e2021GC009807 (2021).
50. Kang, K., Zhong, S., Geruo, A. & Mao, W. The effects of non-Newtonian rheology in the upper mantle on relative sea level change and geodetic observables induced by glacial isostatic adjustment process. *Geophys. J. Int.* **228**, 1975–1991 (2022).
51. Lau, H. C. P. et al. Frequency dependent mantle viscoelasticity via the complex viscosity: cases from Antarctica. *J. Geophys. Res. Solid Earth* **126**, e2021JB022622 (2021).
52. Paxman, G. J. G., Lau, H. C. P., Austermann, J., Holtzman, B. K. & Havlin, C. Inference of the timescale-dependent apparent viscosity structure in the upper mantle beneath Greenland. *AGU Adv.* **4**, e2022AV000751 (2023).
53. Ivins, E. R., Caron, L. & Adhikari, S. Anthropocene isostatic adjustment on an anelastic mantle. *J. Geod.* **97**, 92 (2023).
54. Briner, J. P. et al. Rate of mass loss from the Greenland Ice Sheet will exceed Holocene values this century. *Nature* **586**, 70–74 (2020).
55. Bevis, M. et al. Bedrock displacements in Greenland manifest ice mass variations, climate cycles and climate change. *Proc. Natl Acad. Sci.* **109**, 11944–11948 (2012).
56. Larsen, C. F., Motyka, R. J., Freymeuller, J. T., Echelmeyer, K. A. & Ivins, E. R. Rapid uplift of southern Alaska caused by recent ice loss. *Geophys. J. Int.* **158**, 1118–1133 (2004).
57. Dietrich, R. et al. Rapid crustal uplift in Patagonia due to enhanced ice loss. *Earth Planet. Sci. Lett.* **289**, 22–29 (2010).
58. Ivins, E. R. et al. On-land ice loss and glacial isostatic adjustment at the Drake Passage: 2003–2009. *J. Geophys. Res. Solid Earth* **116**, B02403 (2011).

59. Khan, S. A. et al. Glacier dynamics at Helheim and Kangerdlugssuaq glaciers, southeast Greenland, since the Little Ice Age. *Cryosphere* **8**, 1497–1507 (2014).
60. Brough, S., Carr, J. R., Ross, N. & Lea, J. M. Exceptional retreat of Kangerlussuaq Glacier, East Greenland, between 2016 and 2018. *Front. Earth Sci.* **7**, 123 (2019).
61. Whitehouse, P. L., Gomez, N., King, M. A. & Wiens, D. A. Solid Earth change and the evolution of the Antarctic Ice Sheet. *Nat. Commun.* **10**, 503 (2019).
62. van Calcar, C. J., Bernales, J., Berends, C., van der Wal, W. & van de Wal R. Bedrock uplift reduces Antarctic sea-levelcontribution over next centuries. Preprint.
63. Book, C. et al. Stabilizing effect of bedrock uplift on retreat of Thwaites Glacier, Antarctica, at centennial timescales. *Earth Planet. Sci. Lett.* **597**, 117798 (2022).
64. Vermassen, F. et al. A major collapse of Kangerlussuaq Glacier's ice tongue between 1932 and 1933 in East Greenland. *Geophys. Res. Lett.* **47**, e2019GL085954 (2020).
65. Divine, D. V. et al. Deuterium excess record from a small Arctic ice cap. *J. Geophys. Res. Atmos.* **112**, D19104 (2008).
66. Moresi, L., Dugour, F. & Mühlhaus, H.-B. A Lagrangian integration point finite element method for large deformation modeling of viscoelastic geomaterials. *J. Comput. Phys.* **184**, 476–497 (2003).
67. Sandiford, D., Brune, S., Glerum, A., Naliboff, J. B. & Whittaker, J. M. Kinematics of footwall exhumation at oceanic detachment faults: solid-block rotation and apparent unbending. *Geochem. Geophys. Geosyst.* **22**, e2021GC009681 (2021).
68. Reusen, J. M., Steffen, R., Steffen, H., Root, B. C. & Van der Wal, W. Simulating horizontal crustal motions of glacial isostatic adjustment using compressible Cartesian models. *Geophys. J. Int.* **235**, 542–553 (2023).
69. Tanaka, Y., Klemann, V., Martinec, Z. & Riva, R. E. M. Spectral-finite element approach to viscoelastic relaxation in a spherical compressible Earth: application to GIA modelling. *Geophys. J. Int.* **184**, 220–234 (2011).
70. Spada, G. & Melini, D. SELEN4 (SELEN version 4.0): a Fortran program for solving the gravitationally and. *Geosci. Model Dev.* **12**, 5055–5075 (2019).
71. Mitrovica, J. X., Wahr, J., Matsuyama, I. & Paulson, A. The rotational stability of an ice-age earth. *Geophys. J. Int.* **161**, 491–506 (2005).
72. Mitrovica, J. X. & Wahr, J. Ice age earth rotation. *Annu. Rev. Earth Planet. Sci.* **39**, 577–616 (2011).
73. Conrad, C. P. & Hager, B. H. Spatial variations in the rate of sea level rise caused by the present-day melting of glaciers and ice sheets. *Geophys. Res. Lett.* **24**, 1503–1506 (1997).
74. Farrell, W. Deformation of the Earth by surface loads. *Rev. Geophys.* **10**, 761–797 (1972).
75. Audet, P. Toward mapping the effective elastic thickness of planetary lithospheres from a spherical wavelet analysis of gravity and topography. *Phys. Earth Planteray Inter.* **226**, 48–82 (2014).
76. Gunter, B. C. et al. Empirical estimation of present-day Antarctic glacial isostatic adjustment and ice mass change. *Cryosphere* **8**, 743–760 (2014).
77. Sandberg Sørensen, L. et al. 25 years of elevation changes of the Greenland Ice Sheet from ERS, Envisat, and CryoSat-2 radar altimetry. *Earth Planet. Sci. Lett.* **495**, 234–241 (2018).
78. Valencic, N. et al. Mapping geodetically inferred Antarctic ice surface height changes into thickness changes: a sensitivity study. *Cryosphere* **18**, 2969–2978 (2024).
79. The Danish Agency SDFE, UNAVCO Community and M. Bevis, *Greenland GNSS Network - KUAQ-Kangerdlussuaq Gletscher P.S.*, GPS/GNSS Observations Dataset: The GAGE Facility operated by EarthScope Consortium, https://doi.org/10.7283/HQ0D-3D69 (2009).
80. The Danish Agency SDFE, UNAVCO Community and M. Bevis, *Greenland GNSS Network - MIK2-Mikis Fjord P.S.*, GPS/GNSS Observations Dataset: The GAGE Facility operated by EarthScope Consortium, https://doi.org/10.7283/ABT9-NF76 (2009).
81. The Danish Agency SDFE, UNAVCO Community and M. Bevis, *Greenland GNSS Network - PLPK-Pilappik P.S.*, GPS/GNSS Observations Dataset: The GAGE Facility operated by EarthScope Consortium, https://doi.org/10.7283/QQJP-4H93 (2007).
82. The Danish Agency SDFE, UNAVCO Community and M. Bevis, *Greenland GNSS Network - KSNB-Steenstrup Nordre Brae P.S.*, GPS/GNSS Observations Dataset: The GAGE Facility operated by EarthScope Consortium, https://doi.org/10.7283/RHVV-9P67 (2007).
83. The Danish Agency SDFE, UNAVCO Community and M. Bevis, *Greenland GNSS Network - VFDG-Vestfjord Gletscher P.S.*, GPS/GNSS Observations Dataset: The GAGE Facility operated by UNAVCO, Inc., https://doi.org/10.7283/VT9V-WH52 (2009).
84. The Danish Agency SDFE, UNAVCO Community and M. Bevis, *Greenland GNSS Network - DGJG-Daugaard Jensen Gletshcer P.S.*, GPS/GNSS Observations Dataset: The GAGE Facility operated by EarthScope Consortium, https://doi.org/10.7283/S3EH-XJ14 (2009).
85. International GNNS Service (IGS), *Scoresbysund (SCOR)*, https://gage-data.earthscope.org/archive/gnss/products/position/SCOR (2009).
86. The Danish Agency SDFE, UNAVCO Community and M. Bevis, *Greenland GNSS Network - HEL2-Helheim Glacier P.S*, GPS/GNSS Observations Dataset: The GAGE Facility operated by UNAVCO, Inc., https://doi.org/10.7283/7PB0-2Z53 (2007).
87. The Danish Agency SDFE, UNAVCO Community, K. Larson and T. M. van Dam, *Greenland GNSS Network - KULU-Kulusuk P.S.*, GPS/GNSS Observations Dataset: The GAGE Facility operated by EarthScope Consortium, https://doi.org/10.7283/MF3E-KV11 (1998).
88. Vasskog, K., Langebroek, P. M., Andrews, J. T., Nilsen, J. E. Ø. & Nesje, A. The Greenland Ice Sheet during the last glacial cycle: current ice loss and contribution to sea-level rise from a palaeoclimatic perspective. *Earth-Sci. Rev.* **150**, 45–67 (2015).
89. Lin, Y. et al. A reconciled solution of Meltwater Pulse 1A sources using sea-level fingerprinting. *Nat. Commun.* **12**, 2015 (2021).
90. Gowan, E. J. et al. A new global ice sheet reconstruction for the past 80 000 years. *Nat. Commun.* **12**, 1199 (2021).
91. Kolster, M. E., Døssing, A. & Khan, S. A. Satellite magnetics suggest a complex geothermal heat flux pattern beneath the Greenland Ice Sheet. *Remote Sens.* **15**, 1379 (2023).

Acknowledgements

The authors thank Giorgo Spada and Daniele Melini for making SELEN open source, the authors of the Greenland VMB and ICE-6G_C(VM5a) ice history model for making the data online available, Björn Heyn for his work on making ASPECT and deal.II available on the HPC clusters in Norway, and the Computational Infrastructure for Geodynamics (geodynamics.org), which is funded by the National Science Foundation under award EAR-0949446 and EAR-1550901, for supporting the development of ASPECT. We thank John Naliboff, Rene Gassmöller, Wolfgang Bangerth, and Jacqueline Austermann for contributions that helped to implement GIA capabilities within ASPECT. We thank editor Alireza Bahadori, Fred Richards, Erik Ivins, another anonymous reviewer, and two other anonymous individuals, for comments that improved this manuscript. This work was supported by the Norwegian Research Council projects 288449 (MAGPIE: MFMW & CPC), 223272 (CEED Centre of Excellence: MFMW & CPC) and 332523 (PHAB Centre of Excellence: CPC). Computations were made possible by the Norwegian Research Infrastructure Services (NRIS) via allocations N9283K/NS9029K. The GNSS data is based on services provided by the GAGE Facility, operated by EarthScope, with support from the National Science Foundation, the National Aeronautics and Space Administration, and the U.S. Geological Survey under NSF Cooperative Agreement EAR-1724794.

Author contributions

Conceptualization: MFMW, CPC. Methodology: MFMW. Software: MFMW. Validation: MFMW. Formal analysis: MFMW. Writing—Original Draft: MFMW. Writing—Review & Editing: MFMW, CPC. Visualization: MFMW. Supervision: CPC. Funding Acquisition: CPC.

Competing interests

The authors declare no competing interests.

Additional information

Supplementary information The online version contains supplementary material available at https://doi.org/10.1038/s43247-024-01968-6.

Correspondence and requests for materials should be addressed to Maaike F. M. Weerdesteijn.

Peer review information *Communications Earth & Environment* thanks Erik Ivins, Fred Richards and the other, anonymous, reviewer(s) for their contribution to the peer review of this work. Primary Handling Editor: Alireza Bahadori. A peer review file is available.